The Japan Society
of Applied Physics

RAPID COMMUNICATIONS

Ultrafast spin current generated by electron–magnon scattering in bulk of ferromagnets

To cite this article: Im-Hyuk Shin *et al* 2018 *Jpn. J. Appl. Phys.* **57** 090307

View the article online for updates and enhancements.

You may also like

RAPID COMMUNICATION

Ultrafast spin current generated by electron–magnon scattering in bulk of ferromagnets

Im-Hyuk Shin[1,2], Byoung-Chul Min[1], Byeong-Kwon Ju[2], and Gyung-Min Choi[3]*

[1]Center for Spintronics, Korea Institute of Science and Technology, Seoul 02972, Korea
[2]Display and Nanosystem Laboratory, Korea University, Seoul 02841, Korea
[3]Department of Energy Science, Sungkyunkwan University, Suwon 16419, Korea

*E-mail:gmchoi@skku.edu

The ultrafast demagnetization of metallic ferromagnets can generate a spin current in metallic nonmagnets in a ferromagnet/nonmagnet structure. Two different mechanisms for this phenomenon have been suggested: spin-dependent transport of hot electrons and spin generation by electron–magnon scattering. In this work, we optically measure a transient spin accumulation on a nonmagnetic Cu layer driven by the ultrafast demagnetization of a ferromagnet (Fe, Co, and Ni). The modeling based on the spin generation by electron–magnon scattering in bulk ferromagnets (namely, bulk spin pumping) well explains the dynamics and magnitude of the measured spin accumulation on Cu. © 2018 The Japan Society of Applied Physics

Spin currents have been achieved by applying charge or heat currents to ferromagnets.[1–4] Recently, it has been shown that a pulsed laser injected into a ferromagnetic metal (FM) can generate a spin current to a nonmagnetic, i.e., not ferromagnetic, metal (NM) by the ultrafast demagnetization of FM.[5–14] Experiments on the ultrafast-demagnetization-driven spin current were performed with FM/NM/FM structures by comparing the magnitudes and speeds of the ultrafast demagnetization in the parallel and antiparallel configurations of magnetization.[5,8,9] Another evidence of spin-transfer torque was also observed in the orthogonal configuration of magnetizations.[10,11] Evidence other than the magnetization of FM was obtained from direct measurements of spin accumulation on NM in FM/NM structures using either the second-harmonic generation or the magneto-optical Kerr effect (MOKE).[7,11–13]

Two different explanations were proposed for the physical mechanism of such a spin current driven by the ultrafast demagnetization. The authors of Refs. 6–10, 13, and 14 interpreted their results in terms of the spin-dependent transport of nonthermal electrons, which is called the superdiffusive model.[6] The superdiffusive model predicts that, when nonthermal hot electrons are excited in FM, spin-dependent transport leads to the spin current from FM to NM. This model is a nonthermal analog of the spin-dependent Seebeck effect (SDSE), whose sign and magnitude are determined by the spin-dependent density of states of electrons of FM.[3] Nonthermal processes are expected to play an important role especially when the pulse width of the laser is shorter than the thermalization time of electrons of <100 fs.[15,16] On the other hand, the authors of Refs. 11 and 12 interpreted their results in terms of the spin generation on the electrons of FM by electron–magnon scattering inside the bulk of FM. The generated spins on the electrons of FM can be transferred to the electrons on NM by diffusion (Fig. 1).

Electron–magnon scattering is also the mechanism for the spin Seebeck effect. In ferrimagnetic insulator (FI)/NM structures, the temperature difference between FI and NM excites thermal magnons in FI, and the excited thermal magnons, in turn, generate spin current to NM by electron–magnon scattering at the FI/NM interface.[4,17–19] Theories explain the spin Seebeck effect in terms of spin pumping, which is mediated by *sd* exchange coupling between magnons of FI and electrons of NM at the FI/NM interface.[19–21]
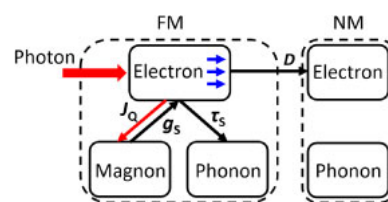

Fig. 1. (Color online) Schematics for bulk spin pumping. The photon energy is initially deposited on the electron bath of FM. The heat transfer (J_Q) (red arrow) from the electron bath to the magnon bath leads to the spin generation on the electron bath at a rate of g_s. The generated spin (blue arrow) on the electron bath of FM is transferred to the electron bath of NM by spin diffusion (D) or to the phonon bath of FM by spin relaxation (τ_s).

A transverse spin Seebeck effect, where the heat and spin currents are orthogonal to each other, was reported with an FM/NM structure, but the anomalous Nernst effect can dominate the signal in the transverse geometry.[22] Note that a theory suggested the spin Seebeck effect, i.e., interfacial spin pumping, as the mechanism for the ultrafast-demagnetization-driven spin current in the FM/NM structure.[23] To distinguish from interfacial spin pumping, we call the spin generation on the electrons of FM by electron–magnon scattering inside the bulk of FM as "bulk spin pumping".

One of the critical distinctions between the spin-dependent transport of electrons and bulk spin pumping is the sign of the spin accumulation on NM. SDSE is an example of the spin-dependent transport of electrons. Previously, different signs of the spin-dependent Seebeck coefficient of [Co/Ni] and [Co/Pt] multilayers were shown to produce different signs of the spin accumulation on Cu at 10 ps and of the spin-transfer torque on another ferromagnet.[12] SDSE originates from the spin-dependent band structure; thus, different signs are allowed. Since the superdiffusive current is a nonthermal version of SDSE, we expect that the sign of the spin polarization driven by the superdiffusive current can vary with FM. However, the sign of the spin polarization by bulk spin pumping is fixed. When the energy of electrons is transferred to magnons, magnon numbers should be increased by magnon excitation. Owing to the angular momentum conservation, the change in angular momentum in the magnon bath should be balanced with the change in angular momentum in the electron bath. Therefore, the sign of the spin polarization of the electron bath should be always positive when energy is transferred from electrons to magnons.

© 2018 The Japan Society of Applied Physics

In this work, we optically measure a transient spin accumulation on Cu driven by the ultrafast demagnetization of FM in the FM/Cu structure and analyze experiments with bulk spin pumping. This model well explains the temporal dynamics and magnitude of the spin accumulation. By quantitative analysis, we obtain the spin relaxation time of FM, which can be compared with the spin diffusion length. Previously, similar experiments were performed with ferromagnetic metals of [Co/Pt] and [Co/Ni] multilayers and ferrimagnetic metals of TbFeCo and GdFeCo alloys,[11,12,24] but the spin diffusion lengths of these complex materials remain unknown. In this work, we use ferromagnetic metals of Fe, Co, and Ni, and the spin relaxation times of these homogenous materials are shown to have a reasonable agreement with the previous reports of the spin diffusion length from the electrical measurement under a steady-state condition.

The sample stacks consist of sap/FM(10)/NM(120)/MgO(3)/Ta(1), where sap is a sapphire substrate with a (0001) orientation, and the numbers in parentheses indicate the thickness of each layer in nanometers. For an FM layer, we use Fe, Co, and Ni for the main investigation and also use [Pt(0.4)/Co(0.2)]$_{\times 17}$ as reference. The Cu layer is selected for NM because of its large spin diffusion length. The MgO and Ta layers are deposited to protect the Cu layer from oxidation. All samples are prepared by magnetron sputtering at a base pressure of $<5 \times 10^{-8}$ Torr.

We measure the dynamics of the demagnetization of FM and spin accumulation on NM using a time-resolved MOKE. Pump light is incident on the FM side of samples through the substrate with an incident fluence of $20 \, \text{J} \, \text{m}^{-2}$. Probe light is incident on either the FM side to detect the demagnetization of FM or the Cu side to detect the spin accumulation on Cu. We use both longitudinal and polar MOKEs. For the longitudinal MOKE, we align the magnetization of FM to the in-plane direction and tilt the incident angle of the probe approximately $10°$ from the normal to the plane. For the polar MOKE, we align the magnetization of FM to the out-of-plane direction and the probe to be normal to the plane. We also measure the temperature evolution using time-domain thermoreflectance (TDTR). The center wavelengths of the pump and probe pulses are 784 nm, and the temporal full-widths at half-maximum are ≈ 1 and ≈ 0.2 ps for the pump and probe, respectively. All measurements are carried out at room temperature.

We first measure the ultrafast demagnetization of FM using the polar MOKE [Fig. 2(a)]. To quantify the amount of the ultrafast demagnetization, the dynamic Kerr rotation is converted to fractional changes in magnetization ($\Delta M/M$) using the static Kerr rotation of each sample. The peak of $\Delta M/M$ is much larger for Ni and [Co/Pt] than for Fe and Co probably because of the much lower Curie temperatures of Ni and [Co/Pt].

We assume that the ultrafast demagnetization of FM originates from the excitations of magnons (waves of spin moments of the local d band), and that the spin loss of the magnon bath leads to the spin gain of the electron bath of FM owing to the conservation of the angular momentum during electron–magnon scattering.[11,25–27] Then, the spin generation rate (g_s) on the electron bath of FM is given by $g_s = -dM/dt$, where dM/dt is the rate of demagnetization [Fig. 2(b)]. Although the probe light can see both the spin loss of the magnon bath (d band) and the spin gain of the electron bath (sp band), we assume that MOKE on the FM side is
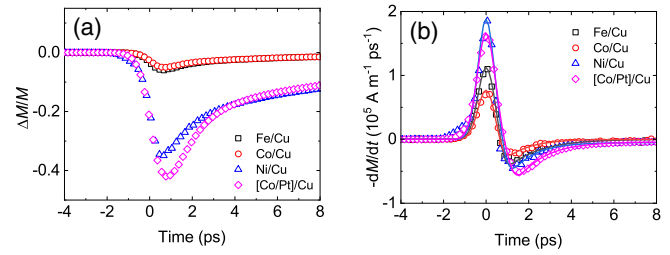

Fig. 2. (Color online) Ultrafast demagnetization of FM. (a) Demagnetization data of the FM(10)/Cu(120) samples measured with the probe beam on the FM side, where FM is Fe (black squares), Co (red circles), Ni (blue triangles), or [Co/Pt] (purple diamonds). (b) Negative of demagnetization rate, $-dM/dt$, for the FM (10 nm)/Cu (120 nm) samples, where FM is Fe (black squares), Co (red circles), Ni (blue triangles), or [Co/Pt] (purple diamonds). Data points are obtained from the time differentiation of demagnetization data of (a), and solid lines are fittings with a Gaussian function.
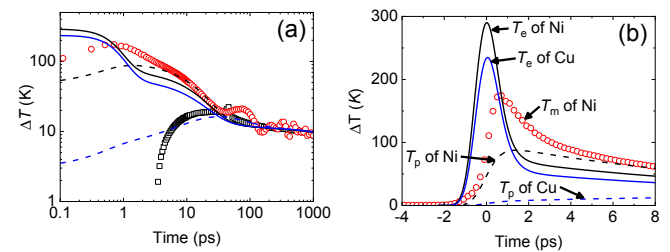

Fig. 3. (Color online) Temperature increase during ultrafast demagnetization. TDTR (black squares) and MOKE (red circles) data of the Ni(10)/Cu(120) sample measured with both pump and probe beams on the Ni side at time scales of (a) 0.1 to 1000 and (b) −4 to 8 ps. Modeling results of the temperatures of Ni electron (black solid line), Ni phonon (black dashed line), Cu electron (blue solid line), and Cu phonon (blue dashed line) with an absorbed fluence of $5.6 \, \text{J} \, \text{m}^{-2}$ per pulse. The Ni temperature is the spatial average of the total Ni thickness, and the Cu temperature is the spatial average of the 10-nm-thick region near the FM/NM interface.

dominated by the spin loss of the magnon bath. This is because, first, the spin–orbit coupling of the d band is larger than that of the sp band, and second, the spin gain of the electron bath of FM rapidly dissipates to the phonon bath of FM and moves to the electron bath of NM.

We consider that magnon excitation is driven by heat transfer among electrons, magnons, and phonons.[25] For thermal analysis, we measure TDTR and MOKE on the Ni side of the Ni/Cu sample at time scales up to 1000 ps [Fig. 3(a)]. The TDTR signal originates from the combination of temperatures of electrons and phonons of Ni and Cu, and the MOKE signal originates from the temperature of magnons of Ni. (The TDTR signal shows a significant deviation from the thermal modeling at a time scale of picoseconds because the signs of the coefficient of thermoreflection of electrons and phonons are opposite for Ni.) After a thermal equilibrium of Ni and Cu at ∼100 ps, TDTR and MOKE data converge. (A small oscillation of the MOKE signal originates from a precession of magnetization driven by a sudden change in anisotropy during the pump pulse.[28]) We normalize TDTR and MOKE by dividing the in-phase signal with the out-phase signal.[29] This method of normalization results in a relative evolution of temperature independent of the pump fluence. To obtain the absolute magnitude of temperature increase, we perform a thermal modeling with an ab-

Table I. Parameters for the spin diffusion calculation in Fig. 4: γ is the electronic heat capacity coefficient, σ is the electrical conductivity, D is the diffusion constant, G is the electrical conductance at the FM/Cu interface, τ_s is the spin relaxation time, and l_s is the spin diffusion length.

	Fe	Co	Ni	[Co/Pt]	Cu
γ (J m^{-3} K^{-2})	690[a]	670[a]	1070[a]	699[b]	100[a]
σ (10^6 Ω^{-1} m^{-1})	3.7[c]	6.7[c]	7.1[c]	2.3[c]	39[c]
D (nm^2 ps^{-1})	130	250	160	80	9500
G (10^{15} Ω^{-1} m^{-2})	2[f]	2[d]	5[e]	2[f]	
τ_s (ps)	0.3	0.2	0.1	0.02	17[g]
l_s (nm)	6	7	4	1	400

a) Obtained from Ref. 34.
b) Obtained from the weighted sum of data of Co and Pt from Ref. 34.
c) Obtained from four-point probe measurements.
d) Obtained from Ref. 35.
e) Obtained from Ref. 36.
f) Assumed to be the same as that of the Co/Cu interface.
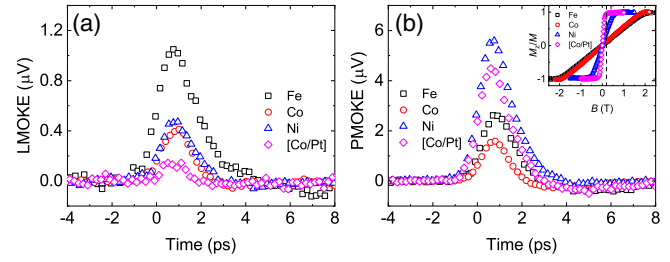g) Estimated from the spin diffusion length of 400 nm in Refs. 37 and 38.

Fig. 4. (Color online) Spin accumulation on Cu. (a) Longitudinal and (b) polar MOKE data of the FM(10)/Cu(120) samples measured with the probe beam on the Cu side, where FM is Fe (black squares), Co (red circles), Ni (blue triangles), or [Co/Pt] (purple diamonds). Inset of (b) is Hysteresis loops of Fe (black squares), Co (red circles), Ni (blue triangles), and [Co/Pt] (purple diamonds) with an out-of-plane magnetic field. The vertical dashed line indicates the magnetic field of 0.2 T.

sorbed pump fluence of 5.6 J m^{-2} (28% of the incident fluence of 20 J m^{-2}) and match experimental data to the modeling results at a time scale of 100–1000 ps. For heat transfer, we use thermal conductivities of 30, 50, and 300 W m^{-1} K^{-1} for sapphire, Ni, and Cu (thermal conductivities of metals are obtained from electrical conductivities and Wiedemann–Franz law), thermal conductances of 0.1 and 40 GW m^{-2} K^{-1} for sapphire/Ni and Ni/Cu interfaces (0.1 GW m^{-2} K^{-1} is the typical value of the phononic thermal conductance and 40 GW m^{-2} K^{-1} is obtained from the electrical conductance of Table I and from the Wiedemann–Franz law), and electron–phonon coupling strengths of 10^{18} and 7×10^{16} W m^{-3} K^{-2} for Ni and Cu, respectively.[30,31] Considering a high electron temperature during the pump pulse, we include the temperature dependence on electronic heat capacity and thermal conductivity in the thermal modeling.

Three different types of heat transfer can generate spins [Fig. 3(b)]. First, the heat transfer between the magnons of FM and the electrons of FM leads to the bulk spin generation on the electrons of FM by bulk spin pumping,

$$ g_s = \frac{2\mu_B}{k_B T} g_{em}(T_{eF} - T_{mF}), \qquad (1) $$

where μ_B is the Bohr magneton, k_B is the Boltzmann constant, g_{em} is the strength of electron–magnon coupling at the bulk of FM, and T_{eF} and T_{mF} are the electron and magnon temperatures of FM, respectively. (We assume that a magnon has an energy $k_B T$ on average.) g_{em} of 6×10^{17} W m^{-3} K^{-1} was reported for Ni.[25] Second, the heat transfer between the magnons of FM and the electrons of NM leads to the interfacial spin generation on the electrons of NM by interfacial spin pumping, i.e., spin Seebeck effect,[19,23]

$$ G_s = \frac{2\mu_B}{k_B T} G_{em}(T_{eN} - T_{mF}), \qquad (2) $$

where G_{em} is the strength of electron–magnon coupling at the FM/NM interface and T_{eN} is the electron temperature of NM. The G_{em} of the FM/NM interface is unknown, and the G_{em} of FI/NM has been reported to be $\approx 10^6$ W m^{-2} K^{-1}.[32] When we compare the G_{em} of 10^6 W m^{-2} K^{-1} with the g_{em} of 6×10^{17} W m^{-3} K^{-1}, $g_{em}h \gg G_{em}$, where h is the ferromagnet thickness of 10 nm. Third, the heat transfer between the electrons

of FM and the electrons of NM leads to the interfacial spin generation on the electrons of NM by SDSE,[3]

$$ G_s = -\left(\frac{\mu_B}{e}\right)\left(\frac{S_s}{L T_{eF}}\right) G_{ee}(T_{eF} - T_{eN}), \qquad (3) $$

where e is the elementary charge, $S_s = [(1 - P^2)/2](S_\uparrow - S_\downarrow)$ is the effective spin-dependent Seebeck coefficient, with P being the spin polarization of the electrical conductivity of FM, and $S_\uparrow$ and $S_\downarrow$ are the Seebeck coefficients of spin-up and spin-down electrons, respectively, L is the Lorenz number (2.45×10^8 W Ω K^{-2}), and G_{ee} is the electronic thermal conductance at the FM/NM interface. The SDSE component can be comparable to that of the ultrafast demagnetization when S_S is $\approx 10 \mu$V K^{-1}.[12] However, we expect that the SDSE contribution would be small for Co since $S_S \approx 1 \mu$V K^{-1} has been reported for Co.[33] In this work, we assume that bulk spin pumping is dominant over the interfacial spin pumping and SDSE.

Next, we measure the spin accumulation on Cu using the longitudinal and polar MOKEs. For the longitudinal MOKE, we fully align the magnetization of FM along the in-plane direction with an external field of 0.1 T, and for the polar MOKE, we partially align the magnetization of FM along the out-of-plane direction with an external field of 0.2 T. The temporal dynamics of the spin accumulation shows a peak at around 0.8 ps and nearly disappears after 3 ps [Fig. 4(a)]. The magnitude of spin accumulation of the Fe/Cu sample is approximately twice as large as those of the Co/Cu and Ni/Cu samples and six times as large as that of the [Co/Pt]/Cu sample. The polar MOKE shows the largest signal with the Ni/Cu structure, which is different from the longitudinal MOKE [Fig. 4(b)]. The discrepancy between the longitudinal and polar MOKE is due to the fact that the out-of-plane magnetic field of 0.2 T tilts the magnetization of FM differently; the relative amounts of the z-component of magnetizations (M_z/M) are 0.1, 0.11, 0.4, and 1 for Fe, Co, Ni, and [Co/Pt], respectively, at the magnetic field of 0.2 T [inset of Fig. 4(b)]. Considering M_z/M, the relative magnitudes of spin accumulation for Fe/Cu, Co/Cu, Ni/Cu, and [Co/Pt]/Cu from the polar MOKE measurements become consistent with those from the longitudinal MOKE.

The raw signal of the polar MOKE in Fig. 4(b) is converted to the spin accumulation as described below. We use three factors: M_z/M, a conversion factor of 0.23 rad V^{-1}, and a conversion factor of 2.5×10^8 A m^{-1} rad^{-1}. M_z/M is deter-
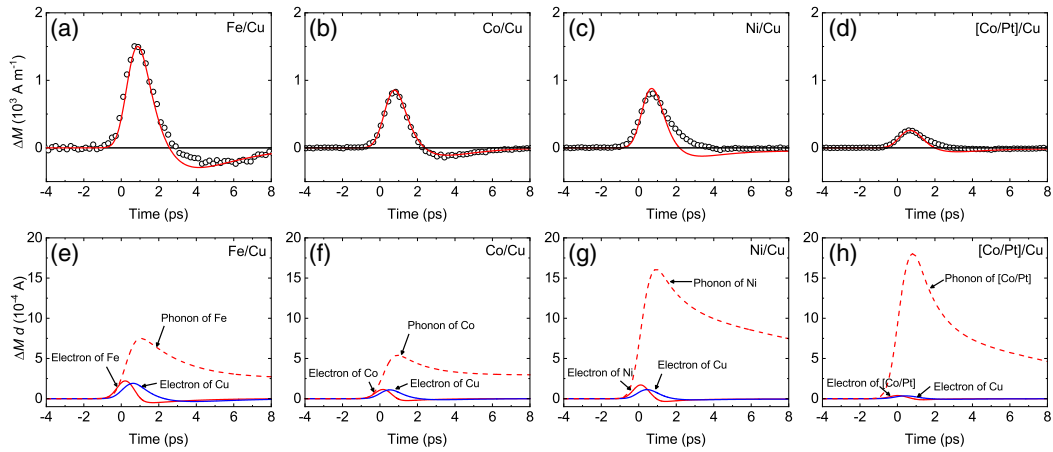
Fig. 5. (Color online) Spin diffusion modeling. Spin accumulation densities (per volume) at the Cu surface side of (a) Fe(10)/Cu(120), (b) Co(10)/Cu(120), (c) Ni(10)/Cu(120), and (d) [Co/Pt](10)/Cu (120) structures: black squares are data points of Fig. 3(b) obtained using conversion factors (see texts); red solid lines are the modeling results based on bulk spin pumping with fitting parameter τ_S values of 0.3, 0.2, 0.1, and 0.02 ps for Fe, Co, Ni, and [Co/Pt], respectively. Units of the y-axis are the same for (a)–(d). Black horizontal lines indicate the y-axis of zero. Thickness-integrated spin accumulation on electrons of FM (red solid lines) and electrons of NM (blue solid lines), and spin dissipation to phonons of FM (red dashed lines) of (e) Fe(10)/Cu(120), (f) Co(10)/Cu(120), (g) Ni(10)/Cu(120), and (h) [Co/Pt](10)/Cu (120) structures. Units of the y-axis are the same for (e)–(h).

mined from the hysteresis loops in the inset of Fig. 4(b). The factor of 0.23 rad V^{-1}, which converts the voltage signal to the Kerr rotation for our polar MOKE system, is determined using a reference sample of 60-nm-thick Co on top of a sapphire substrate. The conversion factor of 2.5×10^8 A m^{-1} rad^{-1} converts the Kerr rotation signal to the spin accumulation signal on Cu.[12] The peaks of the spin accumulation are 1510, 840, 810, and 250 A m^{-1} in the Fe/Cu, Co/Cu, Ni/Cu, and [Co/Pt]/Cu [Figs. 5(a)–5(d)], respectively.

We calculate the spin accumulation density on the NM surface with bulk spin pumping by $g_s = -dM/dt$ and with spin diffusion from FM to NM by

$$\frac{\partial \mu_s}{\partial t} = D \frac{\partial^2 \mu_s}{\partial z^2} - \frac{\mu_s}{\tau_s} + \left(\frac{g_s}{N_s}\right), \qquad (4)$$

where μ_s is the spin chemical potential, D is the spin diffusion constant, τ_s is the spin relaxation time, and N_s is the spin density of states ($N_s = N_F/2$, where N_F is the electronic density of states at the Fermi level, $N_F = \gamma/\pi^2 k_B^2$, with γ being the electronic heat capacity coefficient). D is calculated as $D = \sigma/e^2 N_F$, where σ is the electrical conductivity. The μ_s values of FM and NM are connected at the interface with the interfacial spin conductance $G/2e^2$, where G is the electrical conductance at the interface. We list the γ, σ, D, and G of each layer in Table I.[34–39]

The model of bulk spin pumping well explains the temporal dynamics of the spin accumulation on Cu, especially with Fe and Co: positive peaks at around 0.8 ps and negative peaks at around 3–4 ps (Fig. 5). For the modeling, the only free parameter is τ_s. By the fitting of experiments with modeling, we determine τ_s values of 0.3, 0.2, 0.1, and 0.02 ps, respectively, for Fe, Co, Ni, and [Co/Pt] (Fig. 4). τ_s values of 0.1 and 0.02 ps were reported for [Co/Ni] and [Co/Pt] multilayers, respectively.[12] At a given amount of the ultrafast demagnetization, τ_s and D determine the relative distribution of spins on phonons of FM and electrons of NM [Figs. 5(e)–5(h)]. Initially, spins accumulate on electrons of FM, and then they are transferred to phonons of FM by spin relaxation and to electrons of NM by spin diffusion.

The values of the spin diffusion length l_s, estimated as $l_s = \sqrt{D\tau_s}$, are 6, 7, 4, and 1 nm for Fe, Co, Ni, and [Co/Pt], respectively. Previously, l_s values were determined by electrical measurement under a steady-state condition to be 8.5, 12, >40, 21, and 5.5 nm for Fe, Co$_{91}$Fe$_9$, Co, Ni, and Ni$_{84}$Fe$_{16}$, respectively, at 4 K.[40–45] Considering the temperature dependence on l_s (l_s of Cu and Al at room temperature is about half as large as that at 4–10 K.[37–39]), our results are consistent with the electrical measurements of Fe, Ni$_{84}$Fe$_{16}$, and Co$_{91}$Fe$_9$, but not those of Co and Ni. At the moment, we do not know the reason for the discrepancy between our results and previous electrical measurements of l_s of Co and Ni. Further work, such as that involving temperature-dependent measurements of τ_s, would be required.

In summary, we observe that the ultrafast demagnetization of a ferromagnet of Fe, Co, or Ni induces intense and ultrafast spin accumulation on a nonmagnet of Cu. The dynamics and magnitudes of the spin accumulation are well explained using the model based on the spin generation driven by heat transfer between electrons and magnons of ferromagnets. Our explanation differs from the spin Seebeck effect in that our model considers the electron–magnon scattering inside the bulk of ferromagnetic metals, and it can be named as "bulk spin pumping". Analyzing the spin accumulation results with the bulk spin pumping leads to the determination of the spin relaxation time of ferromagnets. In particular, the spin relaxation time of Fe obtained by our analysis is shown to agree with the spin diffusion length obtained by electrical measurement under a steady-state condition. However, results of the spin relaxation times of Co and Ni do not agree with those of the electrical measurement. Possibly, other thermal mechanisms of the spin-dependent Seebeck effect and interfacial spin pumping might be involved. In addition, nonthermal mechanisms of the superdiffusive current and nonthermal spin pumping can contribute to measurements.

1) M. Johnson and R. H. Silsbee, Phys. Rev. Lett. **55**, 1790 (1985).
2) I. Žutić, J. Fabian, and S. Das Sarma, Rev. Mod. Phys. **76**, 323 (2004).
3) A. Slachter, F. L. Bakker, J.-P. Adam, and B. J. van Wees, Nat. Phys. **6**, 879 (2010).
4) K. Uchida, J. Xiao, H. Adachi, J. Ohe, S. Takahashi, J. Ieda, T. Ota, Y. Kajiwara, H. Umezawa, H. Kawai, G. E. W. Bauer, S. Maekawa, and E. Saitoh, Nat. Mater. **9**, 894 (2010).
5) G. Malinowski, F. Dalla Longa, J. H. H. Rietjens, P. V. Paluskar, R. Huijink, H. J. M. Swagten, and B. Koopmans, Nat. Phys. **4**, 855 (2008).
6) M. Battiato, K. Carva, and P. M. Oppeneer, Phys. Rev. Lett. **105**, 027203 (2010).
7) A. Melnikov, I. Razdolski, T. O. Wehling, E. Th. Papaioannou, V. Roddatis, P. Fumagalli, O. Aktsipetrov, A. I. Lichtenstein, and U. Bovensiepen, Phys. Rev. Lett. **107**, 076601 (2011).
8) D. Rudolf, C. La-o-vorakiat, M. Battiato, R. Adam, J. M. Shaw, E. Turgut, P. Maldonado, S. Mathias, P. Grychtol, H. T. Nembach, T. J. Silva, M. Aeschlimann, H. C. Kapteyn, M. M. Murnane, C. M. Schneider, and P. M. Oppeneer, Nat. Commun. **3**, 1037 (2012).
9) E. Turgut, C. La-o-vorakiat, J. M. Shaw, P. Grychtol, H. T. Nembach, D. Rudolf, R. Adam, M. Aeschlimann, C. M. Schneider, T. J. Silva, M. M. Murnane, H. C. Kapteyn, and S. Mathias, Phys. Rev. Lett. **110**, 197201 (2013).
10) A. J. Schellekens, K. C. Kuiper, R. R. J. C. de Wit, and B. Koopmans, Nat. Commun. **5**, 4333 (2014).
11) G.-M. Choi, B.-C. Min, K.-J. Lee, and D. G. Cahill, Nat. Commun. **5**, 4334 (2014).
12) G.-M. Choi, C.-H. Moon, B.-C. Min, K.-J. Lee, and D. G. Cahill, Nat. Phys. **11**, 576 (2015).
13) M. Hofherr, P. Maldonado, O. Schmitt, M. Berritta, U. Bierbrauer, S. Sadashivaiah, A. J. Schellekens, B. Koopmans, D. Steil, M. Cinchetti, B. Stadtmüller, P. M. Oppeneer, S. Mathias, and M. Aeschlimann, Phys. Rev. B **96**, 100403(R) (2017).
14) A. Alekhin, I. Razdolski, N. Ilin, J. P. Meyburg, D. Diesing, V. Roddatis, I. Rungger, M. Stamenova, S. Sanvito, U. Bovensiepen, and A. Melnikov, Phys. Rev. Lett. **119**, 017202 (2017).
15) L. Guidoni, E. Beaurepaire, and J.-Y. Bigot, Phys. Rev. Lett. **89**, 017401 (2002).
16) N. Bergeard, M. Hehn, S. Mangin, G. Lengaigne, F. Montaigne, M. L. M. Lalieu, B. Koopmans, and G. Malinowski, Phys. Rev. Lett. **117**, 147203 (2016).
17) K. Uchida, H. Adachi, T. Ota, H. Nakayama, S. Maekawa, and E. Saitoh, Appl. Phys. Lett. **97**, 172505 (2010).
18) K. Uchida, T. Ota, H. Adachi, J. Xiao, T. Nonaka, Y. Kajiwara, G. E. W. Bauer, S. Maekawa, and E. Saitoh, J. Appl. Phys. **111**, 103903 (2012).
19) H. Adachi, K.-I. Uchida, E. Saitoh, and S. Maekawa, Rep. Prog. Phys. **76**, 036501 (2013).
20) Y. Tserkovnyak, A. Brataas, and G. E. W. Bauer, Phys. Rev. Lett. **88**, 117601 (2002).
21) Y. Tserkovnyak, A. Brataas, G. E. W. Bauer, and B. I. Halperin, Rev. Mod. Phys. **77**, 1375 (2005).
22) K. Uchida, S. Takahashi, K. Harii, J. Ieda, W. Koshibae, K. Ando, S. Maekawa, and E. Saitoh, Nature **455**, 778 (2008).
23) E. G. Tveten, A. Brataas, and Y. Tserkovnyak, Phys. Rev. B **92**, 180412(R) (2015).
24) G.-M. Choi and B.-C. Min, Phys. Rev. B **97**, 014410 (2018).
25) E. Beaurepaire, J.-C. Merle, A. Daunois, and J.-Y. Bigot, Phys. Rev. Lett. **76**, 4250 (1996).
26) B. Koopmans, G. Malinowski, F. D. Longa, D. Steiauf, M. Fähnle, T. Roth, M. Cinchetti, and M. Aeschlimann, Nat. Mater. **9**, 259 (2010).
27) A. Manchon, Q. Li, L. Xu, and S. Zhang, Phys. Rev. B **85**, 064408 (2012).
28) M. van Kampen, C. Jozsa, J. T. Kohlhepp, P. LeClair, L. Lagae, W. J. M. de Jonge, and B. Koopmans, Phys. Rev. Lett. **88**, 227201 (2002).
29) D. G. Cahill, Rev. Sci. Instrum. **75**, 5119 (2004).
30) A. P. Caffrey, P. E. Hopkins, J. M. Klopf, and P. M. Norris, Microscale Thermophys. Eng. **9**, 365 (2005).
31) W. Wang and D. G. Cahill, Phys. Rev. Lett. **109**, 175503 (2012).
32) J. Kimling, G.-M. Choi, J. T. Brangham, T. Matalla-Wagner, T. Heubner, T. Kuschel, F. Yang, and D. G. Cahill, Phys. Rev. Lett. **118**, 057201 (2017).
33) F. K. Dejene, J. Flipse, and B. J. van Wees, Phys. Rev. B **86**, 024436 (2012).
34) A. Tari, *The Specific Heat of Matter at Low Temperatures* (Imperial College Press, London, 2003).
35) J. Bass and W. P. Pratt, Jr., J. Magn. Magn. Mater. **200**, 274 (1999).
36) C. E. Moreau, I. C. Moraru, N. O. Birge, and W. P. Pratt, Appl. Phys. Lett. **90**, 012101 (2007).
37) F. J. Jedema, M. S. Nijboer, A. T. Filip, and B. J. van Wees, Phys. Rev. B **67**, 085319 (2003).
38) T. Kimura, T. Sato, and Y. Otani, Phys. Rev. Lett. **100**, 066602 (2008).
39) N. Poli, M. Urech, V. Korenivski, and D. B. Haviland, J. Appl. Phys. **99**, 08H701 (2006).
40) D. Bozec, Ph.D. Thesis, Leeds University (2000).
41) A. C. Reilly, W. Park, R. Slater, B. Ouaglal, R. Loloee, W. P. Pratt, Jr., and J. Bass, J. Magn. Magn. Mater. **195**, L269 (1999).
42) A. C. Reilly, W.-C. Chiang, W. Park, S. Y. Hsu, R. Loloee, S. Steenwyk, W. P. Pratt, Jr., and J. Bass, IEEE Trans. Magn. **34**, 939 (1998).
43) C. Moreau, W. P. J. Pratt, and N. O. Birge, Appl. Phys. Lett. **90**, 012101 (2007).
44) S. D. Steenwyk, S. Y. Hsu, R. Loloee, J. Bass, and W. P. Pratt, J. Magn. Magn. Mater. **170**, L1 (1997).
45) J. Bass and W. P. Pratt, J. Phys.: Condens. Matter **19**, 183201 (2007).